Ionics (2017) 23:585–596
DOI 10.1007/s11581-016-1863-2

ORIGINAL PAPER

Influence of co-precipitation temperature on microstructure and electrochemical properties of $Li[Li_{0.2}Mn_{0.54}Ni_{0.13}Co_{0.13}]O_2$ cathode materials for lithium ion batteries

Youxuan Jiang [1,2] · Fei Zhou [1,2] · Chunlei Wang [1] · Jizhou Kong [1,2] · Lipeng Xu [1,2]

Received: 12 June 2016 / Revised: 14 August 2016 / Accepted: 7 October 2016 / Published online: 20 October 2016

Abstract The layered Li-rich Mn-based cathode materials $Li[Li_{0.2}Mn_{0.54}Ni_{0.13}Co_{0.13}]O_2$ were prepared by using co-precipitation technique at different temperatures, and their crystal microstructure and particle morphology were observed and analyzed by XRD and SEM. The electrochemical properties of these samples were investigated by using charge-discharge tests, electrochemical impedance spectroscopy (EIS), and cyclic voltammetry (CV), respectively. The results indicated that all samples are of high purity. When the precursors were co-precipitated at 50 °C, their cathode materials have the most uniform and full particles and exhibit the highest initial discharge capacity (289.4 mAh/g at 0.1C), the best cycle stability (capacity retention rate of 91.2 % after 100 cycles at 0.5C), and the best rate performance. The EIS results show that the lower charge transfer resistance of 50 °C sample is responsible for its superior discharge capacity and rate performance.

Highlights • The Li-rich layered $Li[Li_{0.2}Mn_{0.54}Ni_{0.13}Co_{0.13}]O_2$ powders were synthesized via using a co-precipitation method and a two-step solid-state reaction process.
• All $Li[Li_{0.2}Mn_{0.54}Ni_{0.13}Co_{0.13}]O_2$ samples demonstrate hexagonal α-$NaFeO_2$ structure, and the size of spherical particles varies between 100 and 400 nm.
• The 50 °C sample shows the highest initial discharge capacity (289.4 mAh/g) and the highest initial Coulombic efficiency (81.5 %).
• The 50 °C sample delivers highest discharge capacity at each current density and shows the best rate performance.

✉ Fei Zhou
fzhou@nuaa.edu.cn

[1] State Key Laboratory of Mechanics and Control of Mechanical Structure, Nanjing University of Aeronautics and Astronautics, Nanjing 210016, China

[2] College of Mechanical & Electrical Engineering, Nanjing University of Aeronautics and Astronautics, Nanjing 210016, China

Keywords $Li[Li_{0.2}Mn_{0.54}Ni_{0.13}Co_{0.13}]O_2$ · Co-precipitation temperature · Hexagonal α-$NaFeO_2$ structure · Electrochemical properties

Introduction

To resolve the energy crisis and environment pollution problems caused by the combustion of fossil fuels, the utilization of environment friendly and sustainable green energy sources is a great challenge today. At present, the natural energy resources such as solar energy or wind energy have been paid more attentions, but the intermittence of natural energy resources would make the output of power discontinuity [1]. In order to obtain the continuous output of electronic power, the electronic power produced by natural energy resources should be stored by using different batteries. Now, the battery energy storage has become a main direction of preferred development to integrate intermittent renewable energy into a power grid [2]. In order to reduce the cost and the volume of battery energy storage, it is imperative to develop the cathode materials with high capacity and good cycle and rate performance for lithium ion battery.

In comparison to the traditional cathode materials such as $LiCoO_2$, $LiMn_xNi_yCo_{1-x-y}O_2$, and $LiFePO_4$, Li-excess Mn-based cathode materials $xLi_2MnO_3\cdot(1-x)LiMO_2$(M = Co, Mn, Ni, etc.) possess lower cost, higher capacities (about 250 mAh/g), and higher security and have been widely studied [3–6]. But Li-excess Mn-based cathode materials still have several defects, such as high initial irreversible capacity loss (about 80 mAh/g), low cyclic performance, and poor rate performance, which limit their application in the field of lithium ion battery. Currently, many methods have been used to prepare Li-excess Mn-based cathode materials $xLi_2MnO_3\cdot(1-x)LiMO_2$(M = Co, Mn, Ni, etc.), such as the sol-gel

method [7–9], the co-precipitation method [9–13], the solid reaction method [14], and the combustion reaction method [15, 16]. Among these synthesis methods, carbonate and hydroxide co-precipitation methods have been utilized to synthesize the Li-excess Mn-based cathode materials due to the simple preparation process [9, 13]. As is known, the particle diameter of cathode materials synthesized with carbonate co-precipitation method varied in the range of 2–6 μm [13, 17], while that of cathode materials synthesized by hydroxide co-precipitation method varied in the scope of 0.2–0.5 μm, which could facilitate the diffusion of lithium ion and oxygen evolution during the activation of Li_2MnO_3 component and then enhance the rate performance [9, 12]. Therefore, hydroxide co-precipitation method is suitable to synthesize the hydroxide precursors of transition metal (Mn, Ni, Co). During the co-precipitation process of the hydroxide precursors, $NH_3{\cdot}H_2O$ has been widely used as a chelating agent [12]. Actually, ammonia is not a green chelating agent because of its pungent and choking odor, toxicity, and corrosion, which are harmful to the health of workers. To improve the operation environment of the workers, it is necessary to use an environmentally friendly chelating agent during the co-precipitation process of the hydroxide precursors. In Zhou's group, $C_3H_5NaO_3$ has been used as an environmentally friendly chelating agent, and the corresponding cathode materials demonstrated superior layer structure and capacity retention (higher than 96 % after 100 cycles at 0.5C) [10, 18].

Moreover, to improve the electrochemical performance of Li-excess Mn-based cathode materials, some modification techniques such as doping [19–21] and surface compounds coatings [22–28] have been proposed. In fact, the coating effect and the electrochemical performances of coated materials would be influenced by the morphology, particle size, and electrochemical properties of pristine materials, which were governed by synthetic conditions. When Shi et al. [15] studied the influence of combustion temperature on the electrochemical properties of $Li[Li_{0.2}Mn_{0.54}Ni_{0.13}Co_{0.13}]O_2$ cathode materials prepared via combustion reaction, they found that the cathode materials synthesized at 800 °C had the biggest specific surface area and showed the best rate performance (165.0 mAh/g at current densities 2000 mA/g). Our group has studied the influences of carbonate co-precipitation temperature and stirring time on $Li_{1.2}[Mn_{0.52}Ni_{0.2}Co_{0.08}]O_2$ materials [10] and indicated that if the precursor was prepared at 60 °C/16 h, the corresponding $Li_{1.2}[Mn_{0.52}Ni_{0.2}Co_{0.08}]O_2$ materials demonstrated superior layer structure and low cation mixing degree and delivered the best cycle and rate performance.

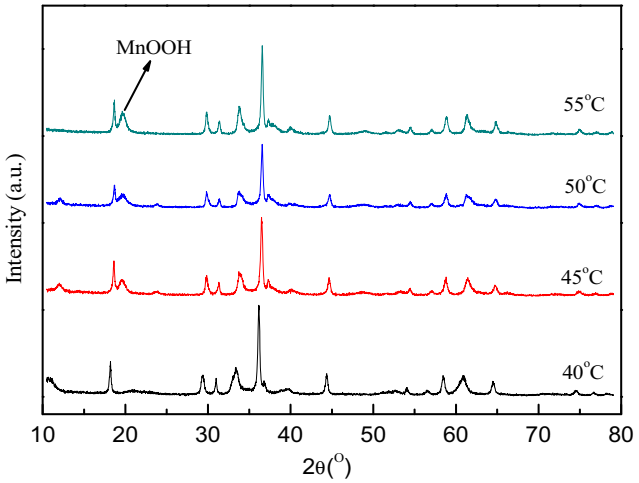

Fig. 2 XRD patterns of $[Mn_{0.54}Ni_{0.13}Co_{0.13}](OH)_{1.6}$ precursors prepared at different co-precipitation temperatures

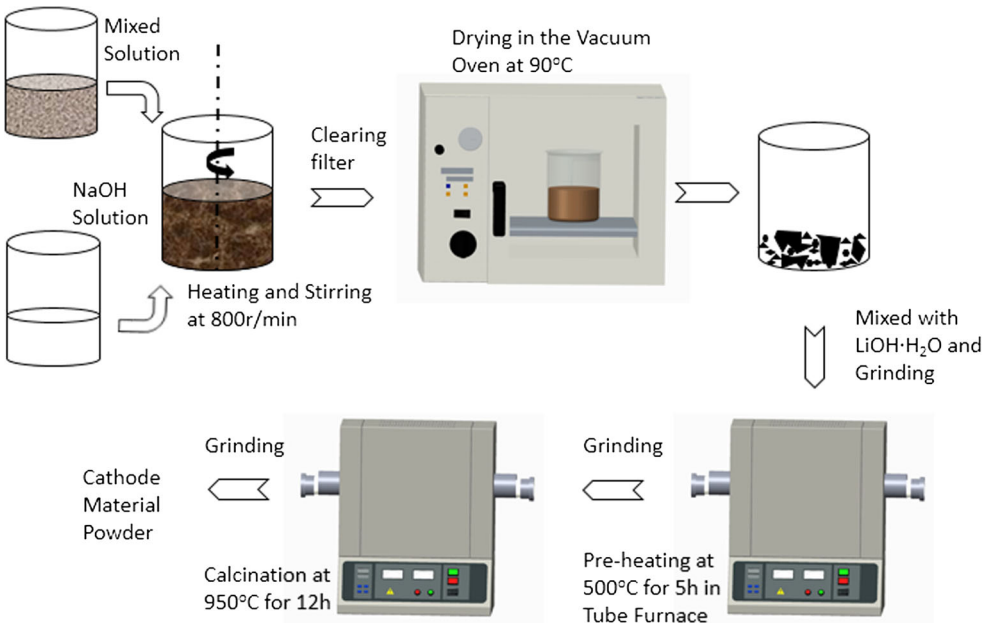

Fig. 1 Schematic diagram of $Li[Li_{0.2}Mn_{0.54}Ni_{0.13}Co_{0.13}]O_2$ synthesized by using the co-precipitation method

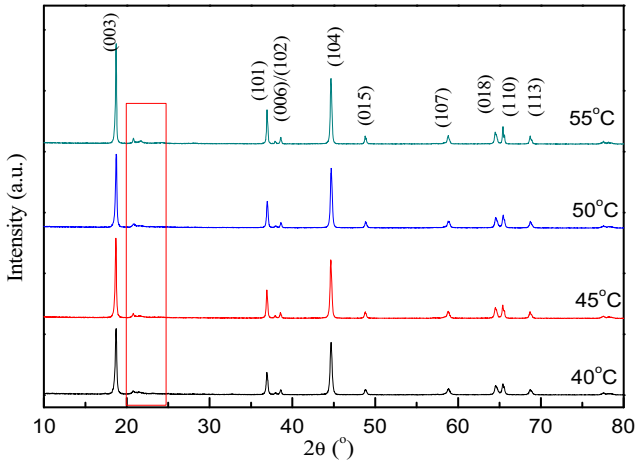

Fig. 3 XRD patterns of $Li[Li_{0.2}Mn_{0.54}Ni_{0.13}Co_{0.13}]O_2$ synthesized at different co-precipitation temperatures

But the synthesis conditions of hydroxide precursors for $Li[Li_{0.2}Mn_{0.54}Ni_{0.13}Co_{0.13}]O_2$ cathode materials are not clear and remain to be discussed.

In here, the $Li[Li_{0.2}Mn_{0.54}Ni_{0.13}Co_{0.13}]O_2$ cathode materials were synthesized with co-precipitation method. NaOH was precipitated, and $C_3H_5NaO_3$ was selected as an ammonia-free chelating agent. And then, the influence of co-precipitation temperatures on the microstructure and electrochemical properties of $Li[Li_{0.2}Mn_{0.54}Ni_{0.13}Co_{0.13}]O_2$ cathode materials was investigated in detail to acquire the optimal co-precipitation temperature.

Experimental details

Preparation of $[Mn_{0.54}Ni_{0.13}Co_{0.13}](OH)_{1.6}$ precursors and $Li[Li_{0.2}Mn_{0.54}Ni_{0.13}Co_{0.13}]O_2$ cathode materials

The Li-rich layered $Li[Li_{0.2}Mn_{0.54}Ni_{0.13}Co_{0.13}]O_2$ powders were synthesized using a co-precipitation method and a two-step solid-state reaction process, which are described in Fig. 1. At first, the stoichiometric amounts of $NiSO_4{\cdot}7H_2O$, $CoSO_4{\cdot}6H_2O$, $MnSO_4{\cdot}H_2O$, and $C_3H_5NaO_3$ chelating agents were dissolved in distilled water, and a mixed solution of 2 mol/L was obtained. After that, the mixed solution and 4 mol/L NaOH solution were simultaneously added dropwise into the reaction caldron in nitrogen condition, respectively. During the synthesis process, the stirring speed was kept at 800 r/min, the pH value was kept at 10.5, and the reaction temperatures were remained at 40, 45, 50, and 55 °C, respectively. After the reaction mixture solution was stirred continuously for 12 h and kept statically for 12 h, the precipitation products were obtained by filtering the reaction mixture solution and cleaned using deionized water to remove the ions of SO_4^{2-}; then, the products were moved into a vacuum chamber to be dried at 100 °C. Soon afterward, the cathode mixture of dried precursors and an excess 5 wt% amount of $LiOH{\cdot}H_2O$ powder was first precalcined at 500 °C for 5 h in air and then calcined at 900 °C for 12 h in air. The prepared cathode oxides were named as 40, 45, 50, and 55 °C samples.

Table 1 $I_{(003)}/I_{(004)}$ ratio and lattice parameter of $Li[Li_{0.2}Mn_{0.54}Ni_{0.13}Co_{0.13}]O_2$ synthesized at different co-precipitation temperatures

Samples (°C)	*a* (Å)	*c* (Å)	*c*/*a*	$I_{(003)}/I_{(104)}$
40	2.8507	14.2230	4.989	1.26
45	2.8515	14.2244	4.988	1.37
50	2.8502	14.2069	4.985	1.24
55	2.8504	14.2271	4.991	1.53

Table 2 Chemical composition of $Li[Li_{0.2}Mn_{0.54}Ni_{0.13}Co_{0.13}]O_2$ synthesized at different co-precipitation temperatures

	Mn (wt%)	Ni (wt%)	Co (wt%)
Theoretical value	34.79	8.95	8.98
40 °C	33.4	9.1	8.6
45 °C	35	9.4	9.1
50 °C	35.4	9.6	9.0
55 °C	35.5	9.4	9.1

Characterization of precursors and cathode materials

The structure of precursors and cathode materials was analyzed using a Rigaku Ultima IV-185 X-ray diffractometer with Cu Kα radiation at 40 kV and 40 mA. And the morphology and the microstructure of precursors and cathode materials were observed using scanning electron microscopy (FE-SEM, JSM-7001F, JEOL). The chemical composition of the cathode materials was measured by using a sequential inductively coupled plasma atomic emission spectrometer (ICPS-8100, made by Shimadzu) with high resolution and sensitivity.

Electrochemical tests of cathode materials

The electrodes were prepared by a slurry coating method. Firstly, the slurry consisting of 80 wt% samples, 10 wt% carbon black, and 10 wt% polyvinylidene fluoride with certain organic solvent 1-methyl-2-pyrrolidone was coated onto Al foils. Secondly, the Al foils were placed in a vacuum and heated at 100 °C for 10 h. Finally, the dried Al foils coated with cathode materials were punched into a circular piece with the diameter of 12 mm. After the 2025-type coin cell which consists of the cathode was used, metal lithium anode separated by a porous polypropylene film (Celgard 2500) was assembled in an argon-filled glove box. One-molar LiPF6 in

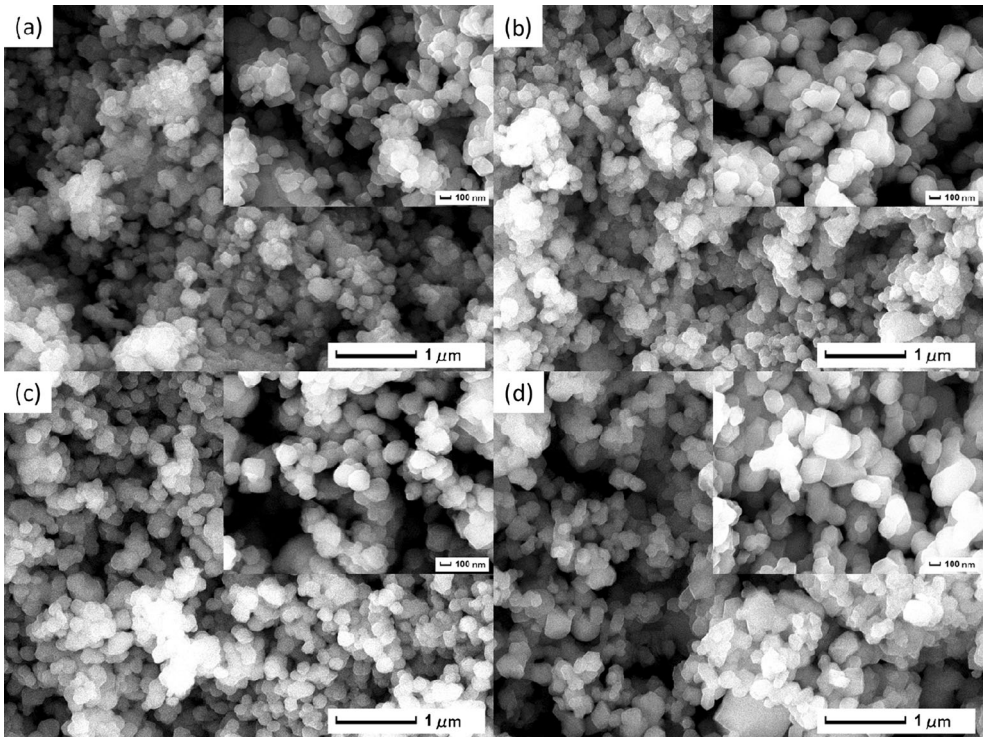

Fig. 4 SEM images of the $Li[Li_{0.2}Mn_{0.54}Ni_{0.13}Co_{0.13}]O_2$ synthesized at the co-precipitation temperatures of 40 °C (**a**), 45 °C (**b**), 50 °C (**c**), and 55 °C (**d**)

1:1 EC/DMC was used as the electrolyte. The galvanostatic charge-discharge tests were performed using the previously mentioned cells on a LAND battery testing system (Wuhan, China). The cells were firstly cycled at a rate of 0.1C (1C = 250 mA/g) for four times with the voltage range from 2.0 to 4.8 V to activate the Li_2MnO_3 phase [29]. After that, the cells were tested at different current densities between 2.0 and 4.6 V. The cyclic voltammetry (CV) of the cells was tested at the voltage range of 2.0–4.8 V and the scan rate of 0.1 mV/s, and the electrochemical impedance spectroscopy (EIS) was measured with a frequency from 0.01 to 100 kHz. Both of the two previously mentioned tests were conducted on an electrochemical workstation (CHI660D).

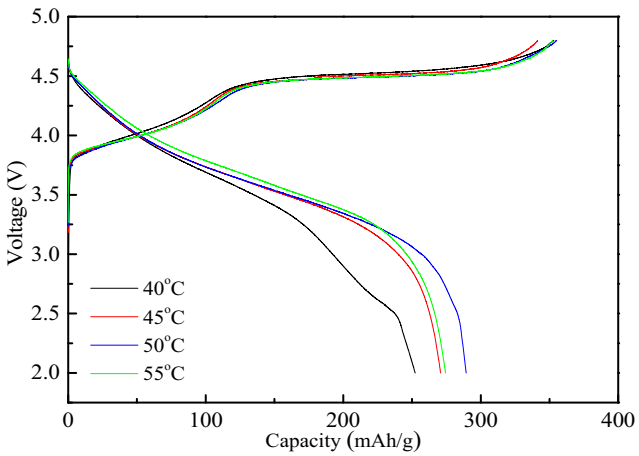

Fig. 5 Initial charge-discharge curves of $Li[Li_{0.2}Mn_{0.54}Ni_{0.13}Co_{0.13}]O_2$ cathode materials in the voltage range of 2.0–4.8 V at 0.1C rate

Results and discussion

Microstructure of $[Mn_{0.54}Ni_{0.13}Co_{0.13}](OH)_{1.6}$ precursors and $Li[Li_{0.2}Mn_{0.54}Ni_{0.13}Co_{0.13}]O_2$ cathode materials

Figure 2 shows the XRD patterns of $[Mn_{0.54}Ni_{0.13}Co_{0.13}](OH)_{1.6}$ precursors prepared at different co-precipitation temperatures (40, 45, 50, 55 °C). It is obvious that all samples show high diffraction peak intensity and integrity peak shape. Meanwhile, the main diffraction peaks of $[Mn_{0.54}Ni_{0.13}Co_{0.13}](OH)_{1.6}$ precursor become sharp with the increment of temperature. This means that the crystal growth and crystallinity become obvious when the co-precipitation temperature increases. In addition, when the co-precipitation temperature is beyond 40 °C, the oxidation peak

Table 3 Initial cycle capacity of $Li[Li_{0.2}Mn_{0.54}Ni_{0.13}Co_{0.13}]O_2$ cathode materials in the voltage range of 2.0–4.8 V

Samples (°C)	Charge capacity (mAh g^{-1})	Discharge capacity (mAh g^{-1})	Irreversible capacity loss (mAh g^{-1})	Coulombic efficiency (%)
40	353.2	252.3	100.9	71.4
45	341.4	270.8	70.6	79.3
50	355.2	289.4	65.8	81.5
55	352.3	274.4	77.9	77.9

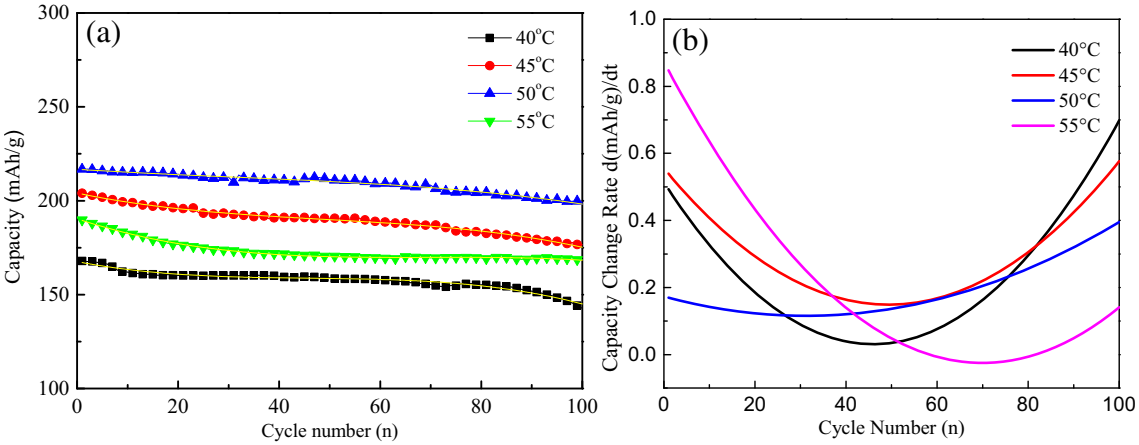

Fig. 6 Cycling performance (**a**) and discharge capacity decay rate (**b**) of $Li[Li_{0.2}Mn_{0.54}Ni_{0.13}Co_{0.13}]O_2$ cathode materials in the voltage range of 2.0–4.6 V at 0.5C rate

of Mn at 19.2° appears and increases gradually. This indicates that $Mn(OH)_x$ is easily oxidized to MnOOH at high temperature [30].

The XRD patterns of $Li[Li_{0.2}Mn_{0.54}Ni_{0.13}Co_{0.13}]O_2$ cathode materials are shown in Fig. 3. No impurity phase is observed in here; this means that all the samples are of high purity [7]. The weak super-lattice peaks located at 20°–25° are an index to the $LiMn_6$ cation arrangement that occurs in the metal layers of Li_2MnO_3 domain, which corresponds to the monoclinic unit cell C2/m [31, 32]. The other diffraction peaks of all four samples could be recognized as hexagonal α-$NaFeO_2$ structure with space group R-3m. Furthermore, the diffraction peaks (006)/(012) and (018)/(110) are separate obviously; this indicates all materials with the well-ordered layered structure [9, 33]. Table 1 shows the lattice parameters and values of $I_{(003)}/I_{(104)}$ for the four samples. As is known, the values of c/a and $I_{(003)}/I_{(104)}$ indicate the stability of layered structure and degree of cation mixing, respectively [34, 35]. As seen in Table 1, the values of c/a ratios and $I_{(003)}/I_{(104)}$ ratios are higher than 4.9 and 1.2, respectively. This points out that all materials exhibit good crystallinity and well-ordered layered structure. The chemical compositions of all samples are listed in Table 2. It is clear that the chemical compositions of all samples are approximately equal to their theoretical value.

Figure 4 shows the SEM images of all samples. It is obvious that all samples are composed of primary particles and secondary particles, and the size of these spherical particles varies in the scope of 100–400 nm. As seen in Fig. 4, the particle size of materials is seriously affected by the co-precipitation temperature. When the co-precipitation temperature is 40 °C, a large number of tiny particles are observed due to the energy shortage. As the co-precipitation temperature rises, the crystallization performance of materials becomes well, and the particles become even (as shown in Fig. 4b). However, as seen in the local magnification of Fig. 4c, the particles of 50 °C sample are more full. With further increasing the temperature to 55 °C, some of the particles are agglomerated together, which results from the abnormal growth of grain.

Electrochemical properties of $Li[Li_{0.2}Mn_{0.54}Ni_{0.13}Co_{0.13}]O_2$ cathode materials

Figure 5 shows the initial charge-discharge curves of the four materials at 0.1C rate between 2.0 and 4.8 V. As seen in Fig. 5, the shapes of charge-discharge curves for all samples are approximately same, but the 50 °C sample shows the highest initial discharge capacity. It is obvious that the charge curves are divided into two processes. The first process at the voltage region from 3.8 to 4.5 V ascribes to the oxidation of Ni^{2+}/Ni^{4+} and Co^{3+}/Co^{4+}. In this process, Li ions are extracted from $LiMO_2$ (M = Ni, Co, Mn) [36, 37]. But, in the second process, a longer voltage plateau is formed, which closely relates to the activation of the layered Li_2MnO_3-like region, and could be found in the initial cycle [38, 39]. This is the reason why these materials can receive a high discharge capacity in the later cycle processes. Table 3 shows the initial charge-discharge capacity, irreversible capacity loss, and Coulombic efficiency of cathode materials prepared at different co-precipitation temperatures. As seen in Table 3, when the co-precipitation temperature rises, the initial Coulombic efficiency first increases to the maximum value of 81.5 % at 50 °C and then reduces to 77.9 %. Actually, when the co-precipitation temperature rises, the crystallization performance becomes well, and then, the aggregation of particles occurs, which would increase the Li^+ diffusion distance [40] and affect the initial Coulombic efficiency.

Figure 6a shows the cycle performance of $Li[Li_{0.2}Mn_{0.54}Ni_{0.13}Co_{0.13}]O_2$ cathode materials at the current density of 125 mAh/g. It is obvious that all materials deliver good cycle performance. The 1st/100th discharge capacities of the four samples are 167.9/142.8, 204.0/176.6, 214.4/195.6, and 204.0/176.6, respectively, and their capacity retention

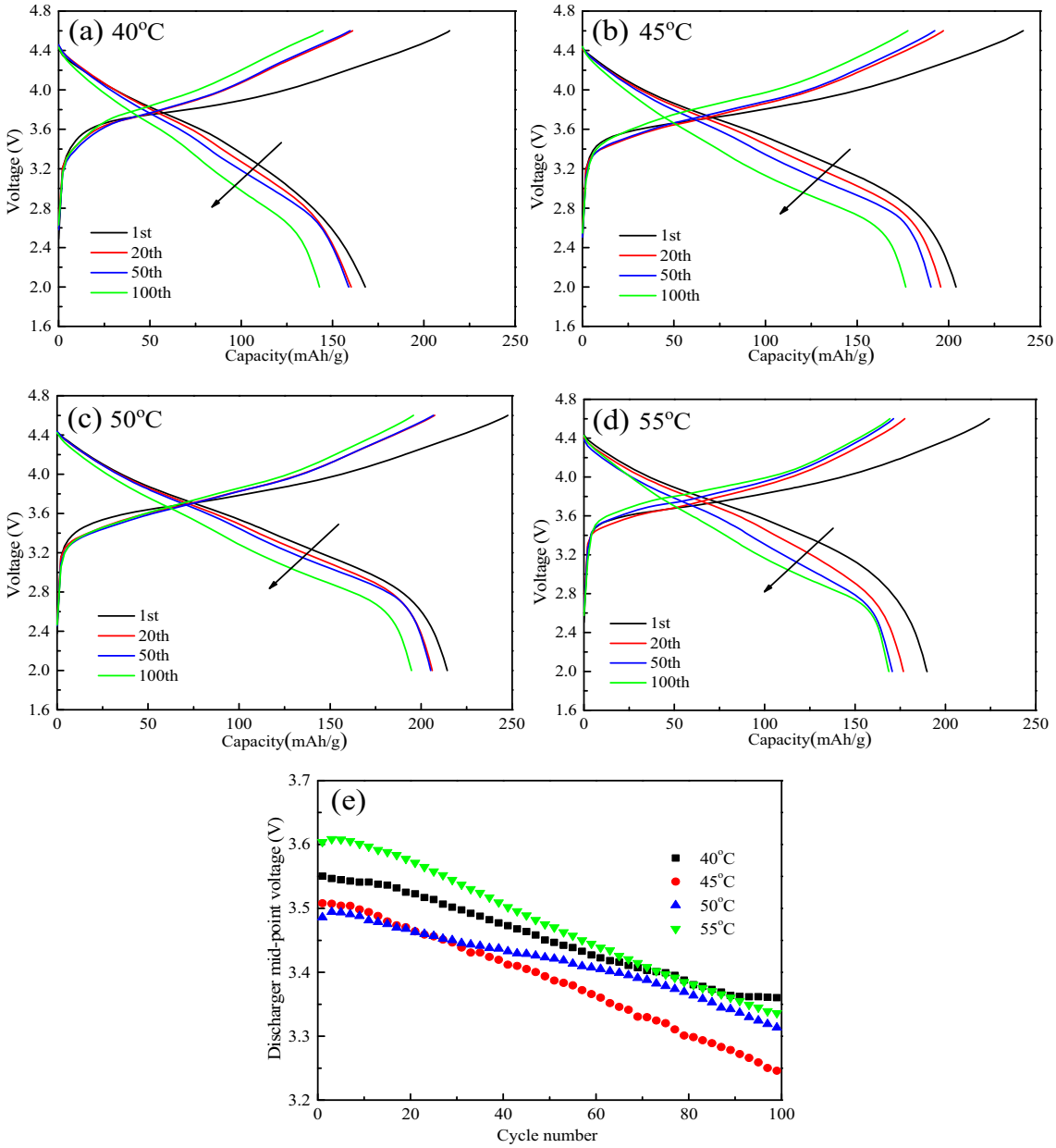

Fig. 7 Charge-discharge profiles and the discharger mid-point potential profiles of $Li[Li_{0.2}Mn_{0.54}Ni_{0.13}Co_{0.13}]O_2$ cathode materials during different cycles at 0.5C rate

rates are 85.1, 86.6, 91.2, and 88.9 %. As seen in Fig. 6a, the cycle-capacity curves are fitted using cubic polynomial with the mean square residuals of 0.97, 0.47, 0.60, and 0.12, respectively, and the fitting functions between the discharge capacity (C) and the cycle number (n) are expressed as follows:

$$C(n) = -7.621 \times 10^{-5} n^3 + 1.051 \times 10^{-2} n^2 - 0.514n + 167.594 \quad (\text{for } 40^{\circ}\text{C sample}) \tag{1}$$

$$C(n) = -5.563 \times 10^{-5} n^3 + 0.824 \times 10^{-2} n^2 - 0.556n + 204.087 \quad (\text{for } 45^{\circ}\text{C sample}) \tag{2}$$

$$C(n) = -1.973 \times 10^{-5} n^3 + 0.185 \times 10^{-2} n^2 - 0.173n + 216.791 \quad (\text{for } 50^{\circ}\text{C sample}) \tag{3}$$

$$C(n) = -6.125 \times 10^{-5} n^3 + 1.285 \times 10^{-2} n^2 - 0.894n + 190.427 \quad (\text{for } 55^{\circ}\text{C sample}) \tag{4}$$

Based on the previously mentioned equations (1–4), the decay rate of discharge capacity with cycle number is represented as $|dC(n)/dn|$. Figure 6b shows the calculation results of $|dC(n)/dn|$. There was a parabolic relationship between the decay rate and the cycle number. It is clear that the discharge

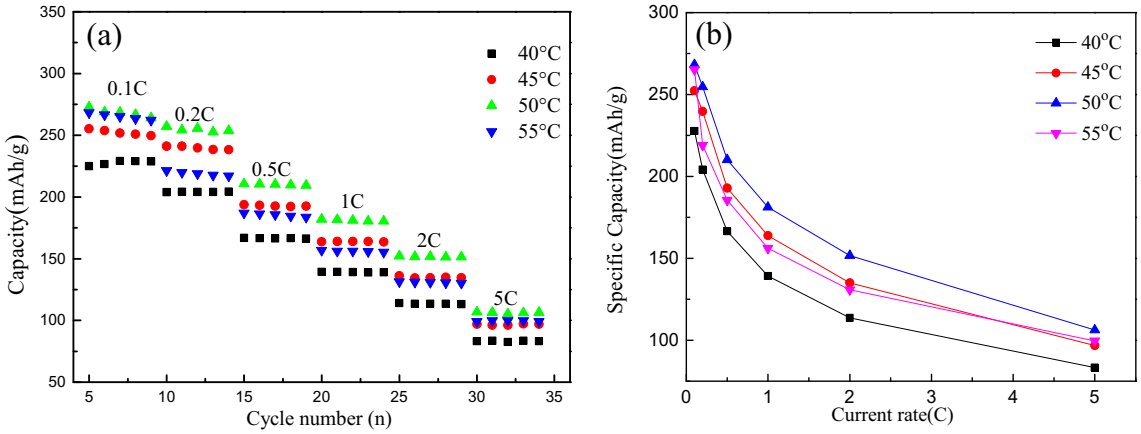

Fig. 8 Rate capability (**a**) and average discharge capacities (**b**) of $Li[Li_{0.2}Mn_{0.54}Ni_{0.13}Co_{0.13}]O_2$ cathode materials at rates of 0.1, 0.2, 0.5, 1.0, 2.0, and 5.0C

capacity for all samples decreases in circulation process, but the discharge capacity decay rate of the 50 °C sample shows the minimum change rate. This indicates that the 50 °C sample shows the best cycle performance and stability. As is known, the LiF is produced by the erosion reaction between hydrogen fluoride (HF) and cathode materials, where HF is generated by the reaction between H_2O and the $LiPF_6$ in electrolyte during the charge-discharge processes. The formation of LiF can hinder the diffusion of lithium ions [30]. Among these cathode materials, the 50 °C sample can resist the erosion of HF more effectively and exhibits the best cycle performance.

Figure 7a–d shows that the charge voltage increases to a high plateau, while the discharge voltage drops to a low plateau when the cycle number increases for all samples; this indicates the enlargement of polarization phenomenon. In addition, discharge midpoint voltage is an important parameter to evaluate the performance of excess Mn-based cathode materials, which reduces with an increase in cycling times and can significantly decrease the power output and restrict its wide application [41]. Figure 7e shows the reducing of discharge midpoint voltage for the four materials with the increment of cycle number. Actually, during the activation process of Li_2MnO_3 and charge/discharge circulation, the vast irreversible appearance of Li_2O will damage the surface structure of the electrode [42]; furthermore, the layered

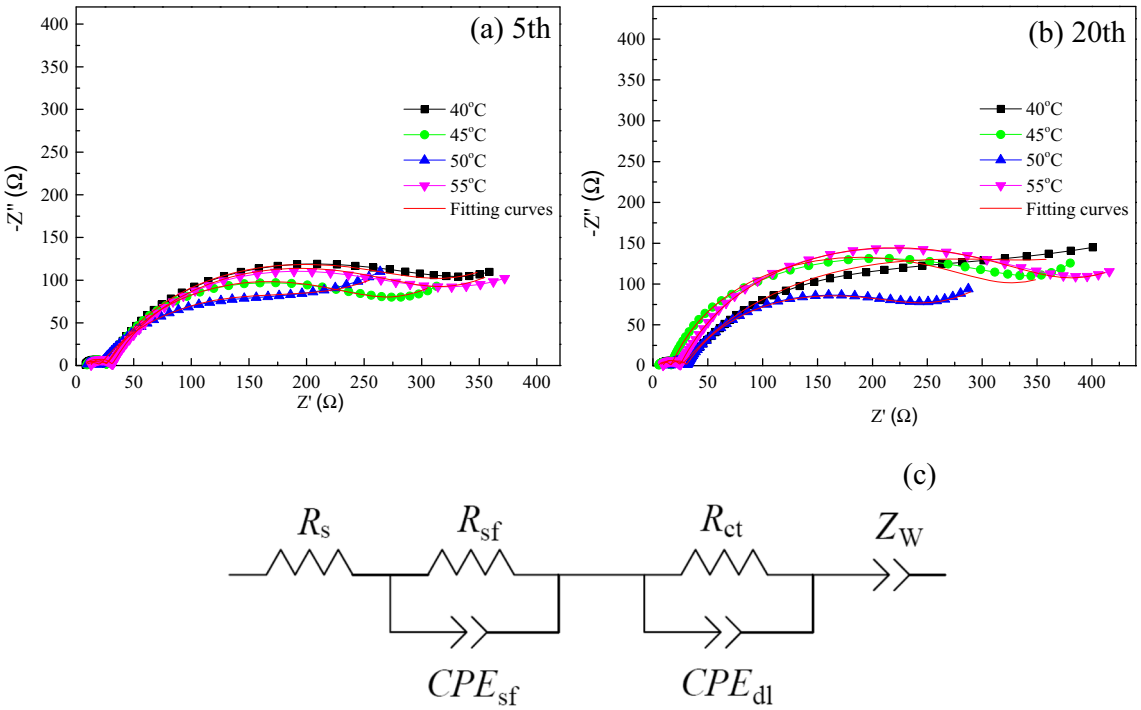

Fig. 9 EIS curves of $Li[Li_{0.2}Mn_{0.54}Ni_{0.13}Co_{0.13}]O_2$ cathode materials at a terminal voltage of 4.5 V in different cycles and the corresponding equivalent circuit

Table 4 Component parameters in equivalent circuit for $Li[Li_{0.2}Mn_{0.54}Ni_{0.13}Co_{0.13}]O_2$ cathode materials at 4.5 V after different cycles

Samples	40 °C		45 °C		50 °C		55 °C	
Cycle number	5th	20th	5th	20th	5th	20th	5th	20th
R_s (Ω)	8.1	6.3	9.3	5.3	8.3	16.2	12.8	9.1
R_{sf} (Ω)	17.5	20.1	16.1	10.1	11.7	13.7	17.8	14.8
n_{sf}	8.5E−1	7.0E−1	8.7E−1	8.9E−1	6.5E−1	8.8E−1	8.6E−1	7.4E−1
Y_{sf} (Ω^{-1} s^{nsf})	8.3E−6	3.8E−5	7.0E−6	5.5E−6	6.0E−5	7.1E−6	8.1E−6	7.4E−6
R_{ct} (Ω)	252.7	315.4	209.9	263.3	171.0	193.0	249.8	310.3
n_{ct}	8.2E−1	7.0E−1	8.3E−1	8.8E−1	7.3E−1	7.8E−1	8.2E−1	8.5E−1
Y_{ct} (Ω^{-1} s^{nct})	3.9E−3	5.8E−3	3.6E−3	2.9E−3	6.4E−3	4.3E−3	3.5E−3	3.2E−3
Y_w (Ω^{-1} $s^{0.5}$)	3.1E−2	3.8E−2	3.5E−2	2.7E−2	3.3E−2	3.8E−2	3.4E−2	3.3E−2

structure is transformed to spinel component and becomes an unexpected layered spinel intergrowth structure [6, 23]; these structure variations would cause the discharge midpoint voltage decreasing. As seen in Fig. 7e, the 55 °C sample shows the highest initial discharge midpoint voltage, due to less activation of Li_2MnO_3 component and thus less discharge capacity delivered below 3.5 V [43]. In order to know their declining slopes more clearly, the data in Fig. 7e can be fitted by linear function, and the corresponding fitting functions between the discharge midpoint voltage (V) and the cycle number (n) are shown as follows:

$$V(n) = -0.21 \times 10^{-2} n + 3.56 \quad (\text{for } 40^{o}\text{C sample}) \tag{5}$$

$$V(n) = -0.27 \times 10^{-2} n + 3.52 \quad (\text{for } 45^{o}\text{C sample}) \tag{6}$$

$$V(n) = -0.17 \times 10^{-2} n + 3.50 \quad (\text{for } 50^{o}\text{C sample}) \tag{7}$$

$$V(n) = -0.30 \times 10^{-2} n + 3.63 \quad (\text{for } 55^{o}\text{C sample}) \tag{8}$$

According to the previously mentioned equations (5–8), the intrinsic discharge midpoint voltage and the declining slope of the 50 °C sample are lowest among the four samples. This indicates that the 50 °C sample shows the best structural stability.

To activate the Li_2MnO_3 phase, the cells were firstly cycled at the current density of 25 mAh/g for four times with the voltage range of 2.0–4.8 V, and then, the rate capabilities of all samples were tested at discharge rates of 0.1C, 0.2C, 0.5C, 1.0C, 2.0C, and 5.0C between 2.0 and 4.6 V, respectively. The test results are shown in Fig. 8. It is distinct that the discharge capacity of the sample reduces when the current density increases from 0.1C to 5.0C. As seen in Fig. 8b, it is obvious that the average rate capacity of the samples decreases markedly with an increase in the current density. When the current density is below 2C, the declining slope of the rate capacity with current density is high, which leads to the rapid decrease of the rate capacity, while that becomes mild at the current density beyond 2C. Furthermore, as the co-precipitation temperature increases, the rate capacity of samples first increases the maximum value at 50 °C and then reduces. This indicates that the 50 °C sample delivers highest discharge capacity and shows the best rate performance.

To understand the effect of co-precipitation temperature on the electrochemical properties of the four samples, the electrochemical impedance spectra (EIS) were measured after charging to 4.5 V in 5th and 20th cycles at the current density of 50 mAh/g and are shown in Fig. 9. It is clear that each curve contains a small semicircle, a large semicircle, and a quasi-

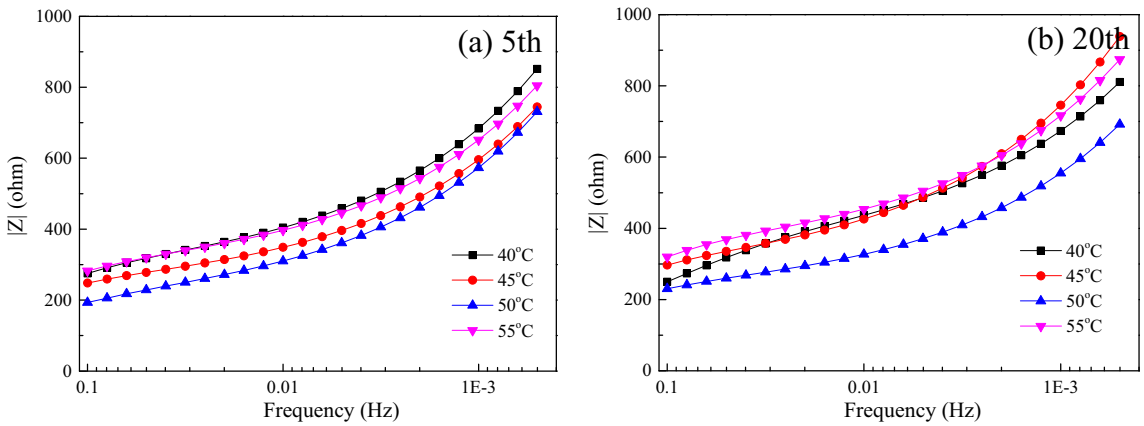

Fig. 10 Impedance of $Li[Li_{0.2}Mn_{0.54}Ni_{0.13}Co_{0.13}]O_2$ cathode materials at a frequency of 0.1~0.0005 Hz in different cycles

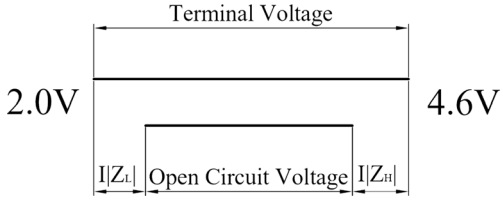

Fig. 11 Schematic diagram of actual voltage range during charge/discharge processes

straight slope. All EIS curves are fitted using the equivalent circuit shown in Fig. 9c. In this equivalent circuit, CPE_{sf} and CPE_{dl} are the constant phase angle elements, while the Warburg impedance (Z_W) is a special constant phase angle element with the phase angle of 45°. They depict the nonideal capacitance of the surface, the nonideal capacitance of the double layer, and the impedance of Li^+ diffusion in the bulk material, respectively. R_s, R_{sf}, and R_{ct} are the ohmic resistance elements and represent the resistance between the working electrode and the reference electrode, the resistance of Li^+ diffusion in the surface layer (solid electrolyte interphase (SEI) layer), and the charge transfer resistance, respectively. The identification results of R_{sf} and R_{ct} for all samples are tabulated in Table 4. It is clear that the values of R_{sf} for the four materials are less than 21 Ω and the values of $|\triangle R_{sf}|$ between 5th and 20th for all samples are less than 7 Ω, which indicate that the SEI layers of the four samples are thin and stable [7]. Moreover, both R_{ct} and $\triangle R_{ct}$ between the 5th and 20th cycles of the 50 °C sample are minimal, showing that the Li-ion diffusion rate at electrode/electrolyte interface for this sample is the fastest. Therefore, the 50 °C sample has the best cycle performance due to the lowest $\triangle R_{ct}$ [8], which is conformed to the results in Fig. 6. Based on the equivalent circuit, the impedance of the battery could be expressed as follows:

$$\left|Z\right| = R_s + \frac{R_{sf}}{\sqrt{1+\left(\omega^{n_{sf}} Y_{sf} R_{sf}\right)^2}} + \frac{R_{ct}}{\sqrt{1+\left(\omega^{n_{ct}} Y_{ct} R_{ct}\right)^2}} + \frac{\omega^{\frac{1}{2}}}{Y_w}, \quad (9)$$

where n and Y are two parameters of constant phase angle element (CPE), Y_w is the parameter of Warburg impedance (Z_W), and ω is equal to $2\pi f$ (f means frequency). In order to understand the impedance characteristics of the battery, the impedances ($|Z|$) of the four samples at different cycles are calculated at the frequency range of 0.1~0.0005 Hz and illustrated in Fig. 10. It is clear that the impedance increases gradually when the frequency decreases. Moreover, the impedance first decreases to the minimum value at 50 °C and then increases when the co-precipitation temperature increases. As seen in Fig. 11, the actual charge/discharge voltage range is, in fact, the interval of open-circuit voltage. In here, $|Z_L|$ and $|Z_H|$ represent the impedances at the minimum/maximum terminal voltage, respectively. When the current density or the impedance increases, the actual charge/discharge range of cell becomes narrow, which causes the decrease of discharge capacity [44]. As seen in Figs. 8 and 10, it is clear that the 50 °C sample delivers the highest discharge capacity and the best rate performance.

As seen in Fig. 12, the good linear relationships between Z' and $\omega^{-1/2}$ at the low frequency region are obtained as follows:

$$Z' = 151.59 + 62.93\omega^{-1/2} \quad (\text{for } 40^{\circ}\text{C sample}) \quad (10)$$

$$Z' = 269.19 + 28.13\omega^{-1/2} \quad (\text{for } 45^{\circ}\text{C sample}) \quad (11)$$

$$Z' = 197.74 + 22.65\omega^{-1/2} \quad (\text{for } 50^{\circ}\text{C sample}) \quad (12)$$

$$Z' = 286.30 + 32.81\omega^{-1/2} \quad (\text{for } 55^{\circ}\text{C sample}) \quad (13)$$

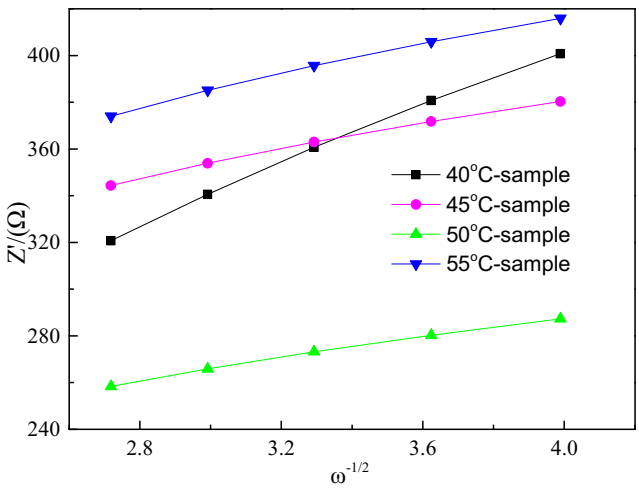

Fig. 12 Relationships between Z' and $\omega^{-1/2}$ in the 20th cycle

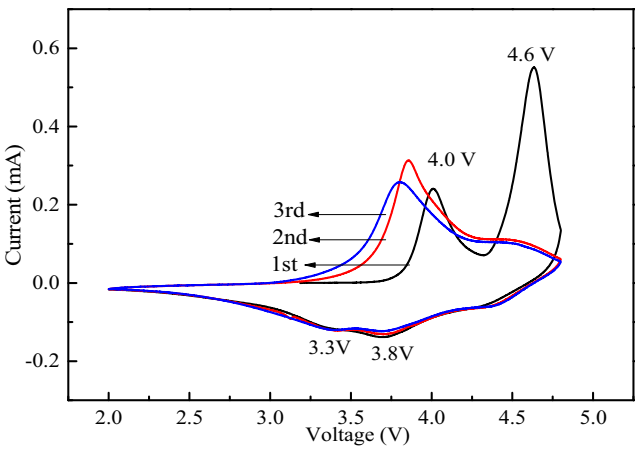

Fig. 13 Cyclic voltammetric profiles of $Li[Li_{0.2}Mn_{0.54}Ni_{0.13}Co_{0.13}]O_2$ synthesized at the co-precipitation temperature of 50 °C

As is known, the Warburg factor (σ) is the slope of the linear fitting equations between Z' and $\omega^{-1/2}$. It is clear that the values of σ for the four samples are 62.93, 28.13, 22.65, and 32.81, respectively. According to [45], the Li^+ diffusion coefficient can be calculated as follows:

$$D_{\mathrm{Li}} = 1/2\left[(RT)/\left(SF^2C\sigma\right)\right]^2 \quad (14)$$

Here, S is the interface area of the cathode/electrolyte (4.524 cm^2), T is the absolute temperature (298 K), R is the gas constant, F is the Faraday constant, and C is the molar concentration of lithium ion [46]. Therefore, D_{Li} is calculated to be 1.57×10^{-15}, 7.74×10^{-15}, 1.21×10^{-14}, and 5.76×10^{-15} $cm^2\ s^{-1}$, respectively. From what we have calculated previously, one can draw a conclusion that the 50 °C sample shows the highest Li-ion diffusion coefficient, which would contribute to improving the capability of cathode materials.

CV has been performed to investigate the redox potential of the transition metal ions in the course of circulation. The three CV curves of the 50 °C sample in the voltage range of 2.0 to 4.8 V with a scanning rate of 0.1 mV/s are shown in Fig. 13. As is known, the oxidation and reduction peaks in the curves correspond to the phase transitions of the cathode materials that occur upon the processes of lithium-ion insertion and extraction. As shown in Fig. 13, the potentials of the redox peaks in the first cycle are quite different toward the remaining two cycles. There are two main oxidation peaks located at about 4.0 and 4.6 V in the CV curves during the initial cycle. The peak at approximately 4.0 V is related to the Ni oxidation from Ni^{2+} to Ni^{4+} and the Co oxidation from Co^{3+} to Co^{4+}. The anodic peak at about 4.6 V is associated with the irreversible electrochemical activation of the Li_2MnO_3; in this reaction, Li_2O is striped from Li_2MnO_3 along with the formation of electrochemically active MnO_2 compound [47]. In the following discharge process, a cathodic peak observed at nearly 3.7 V is ascribed to the reduction reaction of Ni^{4+} to Ni^{2+} and Co^{4+} to Co^{3+}, and the other weak reduction peak at about 3.3 V is assigned to the reaction of Mn^{4+} to Mn^{3+}, which means that the Mn ions in the cathode materials are electrochemically inactive. The CV curves of the second cycle and the third cycle have approximately the same profile. As seen in Fig. 13, the anodic peaks at 4.0 V for the second and third curves shift slightly to the lower-voltage region and the peak at about 4.6 V in the first cycle disappears. In addition, the cathodic peaks at approximately 3.3 V for the second and third cycles become more and more obvious. This suggests that the structure of the materials has changed [7].

Conclusions

The influence of co-precipitation temperature on the microstructure and electrochemical properties of Li-excess Mn-based cathode materials $Li[Li_{0.2}Mn_{0.54}Ni_{0.13}Co_{0.13}]O_2$ has been investigated. The results show that all samples demonstrate hexagonal α-$NaFeO_2$ structure, but the material prepared at 50 °C co-precipitation delivers the most uniform and full particles. Among the four samples, the 50 °C sample shows the highest initial discharge capacity (289.4 mAh/g) and the highest initial Coulombic efficiency (81.5 %). After 100 cycles at 0.5C, the capacity of the 50 °C sample still remains 195.6 mAh/g with the best retention rate (91.2 %). Furthermore, the 50 °C sample delivers the highest discharge capacity and possesses the best rate performance.

Acknowledgments This work was financially supported by the Special Fund of the Scientific and Technological Achievements Transformation Project in Jiangsu Province (No. BA2013142), Jiangsu Province Natural Funds for the Central Universities (No. BK20130800), Fundamental Research Funds for the Central Universities (No. NS2014054), Funding of Shanghai Academy of Spaceflight Technology (No. SAST201371), and Priority Academic Program Development of Jiangsu Higher Education Institutions (PAPD). We would like to acknowledge them for the financial support.

References

1. Nguyen MY, Nguyen DH, Yoon YT (2012) A new battery energy storage charging/discharging scheme for wind power producers in real-time markets. Energies 5:5439–5452
2. Divya KC, Østergaard J (2009) Battery energy storage technology for power systems—An overview. Electr Power Syst Res 79:511–520
3. Shi SJ, Tu JP, Mai YJ, Zhang YQ, Gu CD, Wang XL (2012) Effect of carbon coating on electrochemical performance of Li1.048 Mn0.381 Ni0.286 Co0.286 O2 cathode material for lithium-ion batteries. Electrochim Acta 63:112–117
4. Martha SK, Nanda J, Veith GM, Dudney NJ (2012) Electrochemical and rate performance study of highvoltage lithium-rich composition: Li1.2 Mn0.525 Ni0.175 Co0.1 O2. J Power Sources 199:220–226
5. Croy JR, Gallagher KG, Balasubramanian M, Chen ZH, Ren Y, Kim DH, Kang SH, Dees DW, Thackeray MM (2013) Examining hysteresis in composite xLi2 MnO3 •(1−x)LiMO2 cathode structures. J Phys Chem C 117:6525–6536
6. Mohanty D, Kalnaus S, Meisner RA, Rhodes KJ, Li JL, Payzant EA, Wood DL III, Daniel C (2013) Structural transformation of a lithium-rich Li1.2 Co0.1 Mn0.55 Ni0.15 O2 cathode during high voltage cycling resolved by in situ Xray diffraction. J Power Sources 229:239–248
7. Zhao TL, Chen S, Li L, Zhang XF, Chen RJ, Belharouak I, Wu F, Amine K (2013) Synthesis, characterization, and electrochemistry of cathode material Li[Li0.2 Co0.13 Ni0.13 Mn0.54]O2 using organic chelating agents for lithium-ion batteries. J Power Sources 228:206–213
8. Jin X, Xu QJ, Yuan XL, Zhou LZ, Xia YY (2013) Synthesis, characterization and electrochemical performance of Li[Li0.2 Mn0.54 Ni0.13 Co0.13]O2 cathode materials for lithium-ion batteries. Electrochim Acta 114:605–610

9. Zheng JM, Wu XB, Yang Y (2011) A comparison of preparation method on the electrochemical performance of cathode material Li[Li0.2 Mn0.54 Ni0.13 Co0.13]O2 for lithium ion battery. Electrochim Acta 56:3071–3078
10. Wang CL, Zhou F, Ren C, Wang YF, Kong JZ, Jiang YX, Yan GZ, Li JX (2015) Influences of carbonate coprecipitation temperature and stirring time on the microstructure and electrochemical properties of Li1.2 [Mn0.52 Ni0.2 Co0.08]O2 positive electrode for lithium ion battery. Solid State Ionics 281:96–104
11. Ma SM, Hou XH, Lin ZR, Huang YL, Gao YM, Hu SJ, Shen JD (2016) One-pot facile co-precipitation synthesis of the layered Li1+x (Mn0.6 Ni0.2 Co0.2)1−x O2 as cathode materials with outstanding performance for lithium-ion batteries. J Solid State Electrochem 20:95–103
12. Kong JZ, Ren C, Jiang YX, Zhou F, Yu C, Tang WP, Li H, Ye SY, Li JX (2016) Li-ion-conductive Li2TiO3 -coated Li[Li0.2 Mn0.51 Ni0.19 Co0.1]O2 for high-performance cathode material in lithium-ion battery. J Solid State Electrochem 20:1435–1443
13. Zhu ZY, Zhu LW (2014) Synthesis of layered cathode material 0.5Li2MnO3•0.5LiMn1/3Ni1/3Co1/3O2by an improved co-precipitation method for lithium-ion battery. J Power Sources 256: 178–182
14. Shi SJ, Tu JP, Tang YY, Yu YX, Zhang YQ, Wang XL (2013) Synthesis and electrochemical performance of Li1.131Mn0.504Ni0.243Co0.122O2 cathode materials for lithium ion batteries via freeze drying. J Power Sources 221:300–307
15. Shi SJ, Tu JP, Tang YY, Yu YX, Zhang YQ, Wang XL, Gu CD (2013) Combustion synthesis and electrochemical performance of Li[Li0.2Mn0.54Ni0.13Co0.13]O2with improved rate capability. J Power Sources 228:14–23
16. Kim GY, Yi SB, Park YJ, Kim HG (2008) Electrochemical behaviors of Li[Li(1- x)/3Mn(2- x)/3Nix/3Cox/3]O2cathode series (0<x<1) synthesized by sucrose combustion process for high capacity lithium ion batteries. Mater Res Bull 43:3543–3552
17. Wang CL, Zhou F, Chen KM, Kong JZ, Jiang YX, Yan GZ, Li JX, Yue C, Tang WP (2015) Electrochemical properties of a-MoO3-coated Li[Li0.2Mn0.54Ni0.13Co0.13]O2cathode material for Li-ion batteries. Electrochim Acta 176:1171–1181
18. Wang CL, Zhou F, Ren C, Kong JZ, Tang Z, Li JX, Yu C, Tang WP (2015) Influence of Co increment on the electrochemical properties of Li1.2[Mn0.52−0.5xNi0.2−0.5xCo0.08+x]O2cathode materials for lithium-ion batteries. J Alloys Compd 643:223–230
19. Jin X, Xu QJ, Liu HM, Yuan XL, Xia YY (2014) Excellent rate capability of Mg doped Li[Li0.2Ni0.13Co0.13Mn0.54]O2cathode material for lithium-ion battery. Electrochim Acta 136:19–26
20. Zheng JM, Wu XB, Yang Y (2013) Improved electrochemical performance of Li[Li0.2Mn0.54Ni0.13Co0.13]O2cathode material by fluorine incorporation. Electrochim Acta 105:200–208
21. Qing RP, Shi JL, Xiao DD, Zhang XD, Yin YX, Zhai YB, Gu L, Guo YG (2016) Enhancing the kinetics of Li-Rich cathode materials through the pinning effects of gradient surface Na+Doping. Adv Energy Mater 6:1501914
22. Shi SJ, Tu JP, Tang YY, Liu XY, Zhang YQ, Wang XL, Gu CD (2013) Enhanced cycling stability of Li[Li0.2Mn0.54Ni0.13Co0.13]O2by surface modification of MgO with melting impregnation method. Electrochim Acta 88:671–679
23. Lu C, Wu H, Zhang Y, Liu H, Chen BJ, Wu NT, Wang S (2014) Cerium fluoride coated layered oxide Li1.2Mn0.54Ni0.13Co0.13O2 as cathode materials with improved electrochemical performance for lithium ion batteries. J Power Sources 267:682–691
24. Liu XY, Liu JL, Huang T, Yu AS (2013) CaF2-coated Li1.2Mn0.54Ni0.13Co0.13O2 as cathode materials for Liion batteries. Electrochim Acta 109:52–58
25. Kong JZ, Wang CL, Qian X, Tai GA, Li AD, Wu D, Li H, Zhou F, Yu C, Sun Y, Jia D, Tang WP (2015) Enhanced electrochemical performance of Li1.2Mn0.54Ni0.13Co0.13O2 by surface modification with graphene-like lithium-active MoS2. Electrochim Acta 174:542–550
26. Cong LN, Gao XG, Ma SC, Guo X, Zeng YP, Tai LH, Wang RS, Xie HM, Sun LQ (2014) Enhancement of electrochemical performance of Li[Li0.2Mn0.54Ni0.13Co0.13]O2by surface modification with Li4Ti5O12. Electrochim Acta 115:399–406
27. Wang ZY, Liu EZ, He CN, Shi CS, Li JJ, Zhao NQ (2013) Effect of amorphous FePO4 coating on structure and electrochemical performance of Li1.2Ni0.13Co0.13Mn0.54O2 as cathode material for Li-ion batteries. J Power Sources 236:25–32
28. Zheng FH, Yang CH, Xiong XH, Xiong JW, Hu RZ, Chen Y, Liu ML (2015) Nanoscale surface modification of lithium-rich layered-oxide composite cathodes for suppressing voltage fade. Angew Chem Int Ed 54:13058–13062
29. Yan PF, Xiao L, Zheng JM, Zhou YG, He Y, Zu XT, Mao SX, Xiao J, Gao F, Zhang JG, Wang CM (2015) Probing the degradation mechanism of Li2MnO3Cathode for Li-ion batteries. Chem Mater 27:975–982
30. Yabuuchi N, Yoshii K, Myung ST, Nakai I, Komaba S (2011) Detailed studies of a high-capacity electrode material for rechargeable batteries, Li2MnO3-LiCo1/3Ni1/3Mn1/3O2. J Am Chem Soc 133:4404–4419
31. Thackeray MM, Kang SH, Johnson CS, Vaughey JT, Benedek R, Hackney SA (2007) Li2MnO3-stabilized LiMO2(M = Mn, Ni, Co) electrodes for lithium-ion batteries. J Mater Chem 17:3112–3125
32. Yoon WS, Iannopollo S, Grey CP, Carlier D, Gorman J, Reed J, Ceder G (2004) Local structure and cation ordering in O3 lithium nickel manganese oxides with stoichiometry LiNiXMn(2-x)/3Li(1-2x)/3O2. Electrochem Solid State Lett 7(7):A167–A171
33. Li J, Klopsch R, Stan MC, Nowak S (2011) Synthesis and electrochemical performance of the high voltage cathode material Li[Li0.2Mn0.56Ni0.16Co0.08]O2with improved rate capability. J Power Sources 196:4821–4825
34. Cho SW, Kim GO, Ryu KS (2012) Sulfur anion doping and surface modification with LiNiPO of a Li[Co0.1Ni0.15Li0.2Mn0.55]O2 cathode material for Li-ion batteries. Solid State Ionics 206:84–90
35. Nobili F, Croce F, Tossici R, Meschini I (2012) Sol–gel synthesis and electrochemical characterization of Mg-/Zr-doped LiCoO2cathodes for Li-ion batteries. J Power Sources 197:276–284
36. Kang SH, Thackeray MM (2009) Enhancing the rate capability of high capacity xLi2MnO3•(1-x)LiMO2(M =Mn, Ni, Co) electrodes by Li–Ni–PO4 treatment. Electrochem Commun 11:748–751
37. Yi TF, Tao W, Chen B, Zhu YR, Yang SY, Xie Y (2016) High-performance xLi2MnO3(1-x) LiMn1/3Co1/3Ni1/3O2(0.1<x<0.5) as cathode material for lithium-ion battery. Electrochim Acta 188: 686–695
38. Robertson AD, Bruce PG (2002) The origin of electrochemical activity in Li2MnO3. Chem Commun 2790–2791
39. Thackeray MM, Johnson CS, Vaughey JT, Li N, Hackney SA (2005) Advances in manganese-oxide 'composite' electrodes for lithium-ion batteries. J Mater Chem 15:2257–2267
40. Yabuuchi N, Kubota K, Aoki Y, Komaba S (2016) Understanding particle-size-dependent electrochemical properties of Li2MnO3-Based positive electrode materials for rechargeable lithium batteries. J Phys Chem C 120:875–885
41. Croy JR, Kim D, Balasubramanian M, Gallagher K, Kang SH, Thackeray MM (2012) Countering the voltage decay in high capacity xLi2MnO3•(1–x)LiMO2Electrodes (M=Mn, Ni, Co) for Li+−Ion batteries. J Electrochem Soc 159:A781–A790
42. Ito A, Li DC, Sato Y, Arao M, Watanabe M, Hatano M, Horie H, Ohsawa Y (2010) Cyclic deterioration and its improvement for Li-rich layered cathode material Li[Ni0.17Li0.2Co0.07Mn0.56]O2. J Power Sources 195:567–573

43. Lu ZH, Dahn JR (2002) Understanding the anomalous capacity of Li/Li[NixLi(1/3−2x/3)Mn(2/3−x/3)]O2Cells using in situ x-ray diffraction and electrochemical studies. J Electrochem Soc 149:A815–A822
44. Karthikeyana K, Amaresha S, Lee GW, Aravindana V, Kim H, Kang KS, Kim WS, Lee YS (2012) Electrochemical performance of cobalt free, Li1.2 (Mn0.32Ni0.32Fe0.16)O2cathodes for lithium batteries. Electrochim Acta 68:246–253
45. Zhang JC, Zhang H, Gao R, Li ZY, Hu ZB, Liu XF (2016) New insights into the modification mechanism of Li-rich Li1.2Mn0.6Ni0.2O2 coated by Li2ZrO3. Phys Chem Chem Phys 18:13322–13331
46. Li LJ, Chen ZY, Zhang QB, Xu M, Zhou X, Zhu HL, Zhang KL (2015) A hydrolysis-hydrothermal route for the synthesis of ultrathin LiAlO2-inlaid LiNi0.5Co0.2Mn0.3O2 as a high-performance cathode material for lithium ion batteries. Mater Chem A 3:894–904
47. Johnson CS, Li NC, Lefief C, Vaughey JT, Thackeray MM (2008) Synthesis, characterization and electrochemistry of lithium battery electrodes: xLi2MnO3•(1 - x)LiMn0.333Ni0.333Co0.333O2(0<=x<=0.7). Chem Mater 20:6095–6106